Object Detection Aided GNSS and Its Integration with LiDAR in Highly Urbanized Areas

Weisong Wen, Guohao Zhang, Li-Ta Hsu

***Abstract*—Positioning is a key function for autonomous vehicles that requires globally referenced localization information. LiDAR-based mapping, which refers to the simultaneous localization and mapping (SLAM), provides continuous positioning in diverse scenarios. However, the error of SLAM can accumulate over time. Besides, only relative positioning is provided by SLAM. Global navigation satellites system (GNSS) receiver is one of the significant sensors for providing globally referenced localization and is usually integrated with LiDAR in autonomous driving. However, the performance of GNSS is severely challenged due to the reflection and blockage of the buildings in super-urbanized cities, including Hong Kong and Tokyo and New York, causing the notorious non-line-of-sight (NLOS) receptions. Moreover, the uncertainty of GNSS positioning is ambiguous resulting in the incorrect tuning of its weight during the GNSS/LiDAR integration. Innovatively, this paper employs a LiDAR to identify the NLOS measurement of GNSS receiver using the point-cloud based object detection. Measurements from satellites suffered from NLOS reception will be excluded based on the proposed fault detection and exclusion (FDE) algorithm. Then, the GNSS weight least square positioning is conducted based on the survived measurements from the FDE. The noise covariance of GNSS positioning is calculated by considering the potential positioning errors caused by NLOS and remaining line-of-sight (LOS) measurements. The improved GNSS result and its corresponding noise covariance are integrated with the LiDAR using a graph-based SLAM integration framework. Experimental results indicate that the proposed GNSS/LiDAR integration can obtain improved positioning accuracy in a highly-urbanized area in Hong Kong.**

***Index Terms*—GNSS; LiDAR; Integration; SLAM; Adaptive tuning; Urban canyon**

I. Introduction

Autonomous vehicles [1, 2] receive increasing attention due to its immense potential market. To fully activate autonomous vehicles, the globally referenced and meter-level positioning is required in all scenarios. LiDAR is a commonly used sensor for autonomous driving which is not only be used for object detection [3, 4] and also is employed to provide continuous positioning [5]. In LiDAR-based positioning, the SLAM [6, 7] algorithm is usually employed to calculate the transformation between the consecutive point clouds provided by LiDAR. However, the localization from the SLAM can introduce accumulated error over time, and only relative positioning is obtained which cannot satisfy the requirement of the autonomous vehicles. With the rise of multi-GNSS, the availability of satellites has been significantly enhanced, which makes it possible to receive enough satellites for GNSS positioning even in an urban canyon. GNSS is currently a significant source providing the continuous global positioning. It is usually integrated with the LiDAR-based localization to take advantages of both positioning sources [8-12]. Based on the principle of sensor fusion, the sensor integration methods can be divided into two groups, the filtering-based and the smoothing-based integrations. The symbolic filtering based sensor integration method is the Bayes filter, including Kalman filter [13, 14], information filter [15-17] and particle filter [18-20]. The Bayes filter-based sensor integration estimates current state based on current observation and the previous state estimation, failing to make use of all the states before the previous states. This is because of the assumption of the first order of the Markov model [21] which is one of the key assumptions of the Bayes filter. Conversely, the smoothing approaches [22-25] estimate the pose and map by considering the full sets of measurements from the first epoch to current epoch. The most well-known smoothing method is the graph-based SLAM [26]. These GNSS/LiDAR integration solutions can obtain decent positioning performance in sparse areas as shown in Fig. 1. However, performance can be severely challenged in the super-urbanized area due to poor performance and large uncertainty in GNSS positioning. GNSS can achieve 5~10 meters regarding positioning accuracy in an open area or sparse scenarios base on the conventional single point positioning (SPP). However, the positioning error can significantly increase to ~50 meters in super-urbanized areas [27], due to the reflection and blockage from the surrounding buildings. The reflection can cause extra travel delay in the

This work was supported in part by the Hong Kong Polytechnic University internal grant G-YBWB under Fund for ECS Project Rated 3.5 (CRG)."

W. Wen, G. Zhang and L.-T. Hsu are with, The Hong Kong Polytechnic University, Kowloon, Hong Kong. (e-mail: 17902061r@connect.polyu.hk; guohao.zhang@connect.polyu.hk; lt.hsu@polyu.edu.hk).

pseudorange domain, thus causing the well-known multipath effects and NLOS receptions. Moreover, the uncertainty of the GNSS positioning is also greatly increased due to the severe NLOS.

According to a recent survey [28], the NLOS is the dominant component to blame for positioning error in dense urban areas. Numerous studies [29-33] are conducted to identify the NLOS receptions. Due to NLOS is caused by the reflection from buildings, the 3D city models are employed to identify the NLOS receptions [34-39]. With the aided of the 3D city models, the possible blockage from the buildings can be detected, and the corresponding NLOS is obtained. Then the NLOS measurements are excluded from the GNSS positioning subsequently. However, this method relies heavily on the availability of the 3D city models which is the main problem for its implementation. The range-based 3D map aided GNSS (3DMA GNSS) [29, 31-33] is one of the most mature techniques to mitigate the positioning errors from NLOS receptions. It innovatively employs the ray-tracing simulation to simulate the possible transmission routes of the GNSS signals. Thus, the travel delay can be calculated based on the simulated signal transmission route. The NLOS measurement is also corrected and used in the further GNSS positioning calculation. However, this method introduces a heavy computational load due to the ray-tracing simulation. Moreover, 3D city models are also needed, and those map-aided GNSS positioning methods rely heavily on the initial guess of the receiver.

The other problem in GNSS/LiDAR integration is the large uncertainty of GNSS positioning in urbanized areas. The uncertainty is referred to as the noise covariance which is essential in the GNSS/LiDAR integration. Satisfactory performance can be obtained using the GNSS/LiDAR integration scheme on the condition that each sensor noises are well modeled. However, the researches in [8-10, 12] model the GNSS positioning uncertainty as Gaussian distribution. This rough modeling of GNSS positioning uncertainty can work in the places where GNSS positioning is robust and accurate with few NLOS receptions. However, the GNSS positioning error does not subject to Gaussian distribution any more in the urbanized area [27]. The conventional constant and Gaussian distribution-based covariance cannot model the actual performance of the GNSS positioning. As a result, the GNSS/LiDAR integration result can introduce additional positioning error. A GNSS covariance estimation solution based on satellites numbers and signal to noise ratio (SNR) which can obtain improvements [40] comparing with the conventional constant covariance solution. However, this scheme cannot effectively model the positioning error from NLOS. Taking advantage of the 3D LiDAR sensor, the 3D point cloud map is employed to identify the NLOS measurement [41]. This method can effectively detect the NLOS signals which are similar to the methods in [35, 42] using the 3D city models. Then, the NLOS receptions are all excluded from the GNSS positioning. The point cloud map plays a similar role of the 3D city maps. However, this implementation of this method is subjected to the availability of the fully 3D point cloud map of buildings, which is difficult to obtain. Moreover, the GNSS positioning uncertainty is simply estimated based on the new horizontal dilution of precision (HDOP), and the actual NLOS errors are not effectively modeled.

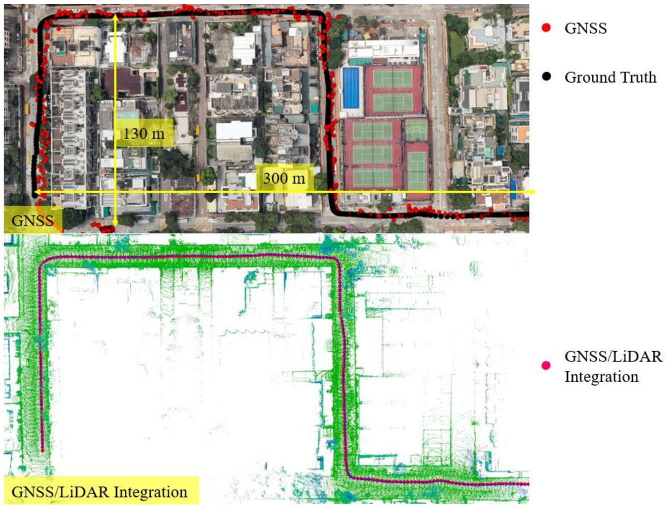

Fig. 1. The top panel shows the performance of GNSS standalone positioning. The red circle indicates the GNSS positioning result and black circle is with respect to the ground truth. The bottom panel shows the GNSS/LiDAR integration, where the green points represent the point cloud map and the pink circles represent the trajectory generated by GNSS/LiDAR integration.

Fig. 2 demonstrates a highly urbanized scenario in Hong Kong, with both sides being filled with tall buildings. As a result, the GNSS receiver can receive lots of NLOS measurements which only contains the reflected signals.

This paper innovatively employs the 3D LiDAR to facilitate the GNSS positioning and corresponding covariance estimation using the real-time point clouds-based object detection. Then, the improved GNSS positioning is integrated with LiDAR odometry under a graph-based SLAM framework. The

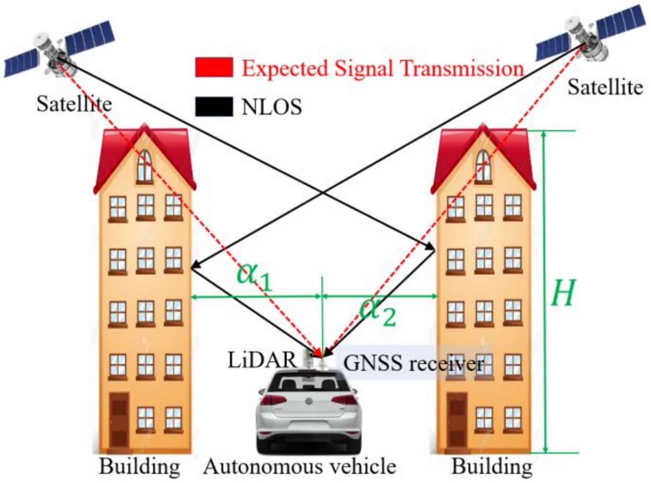

Fig. 2. The demonstration of NLOS receptions of GNSS receiver caused by the surrounding buildings.

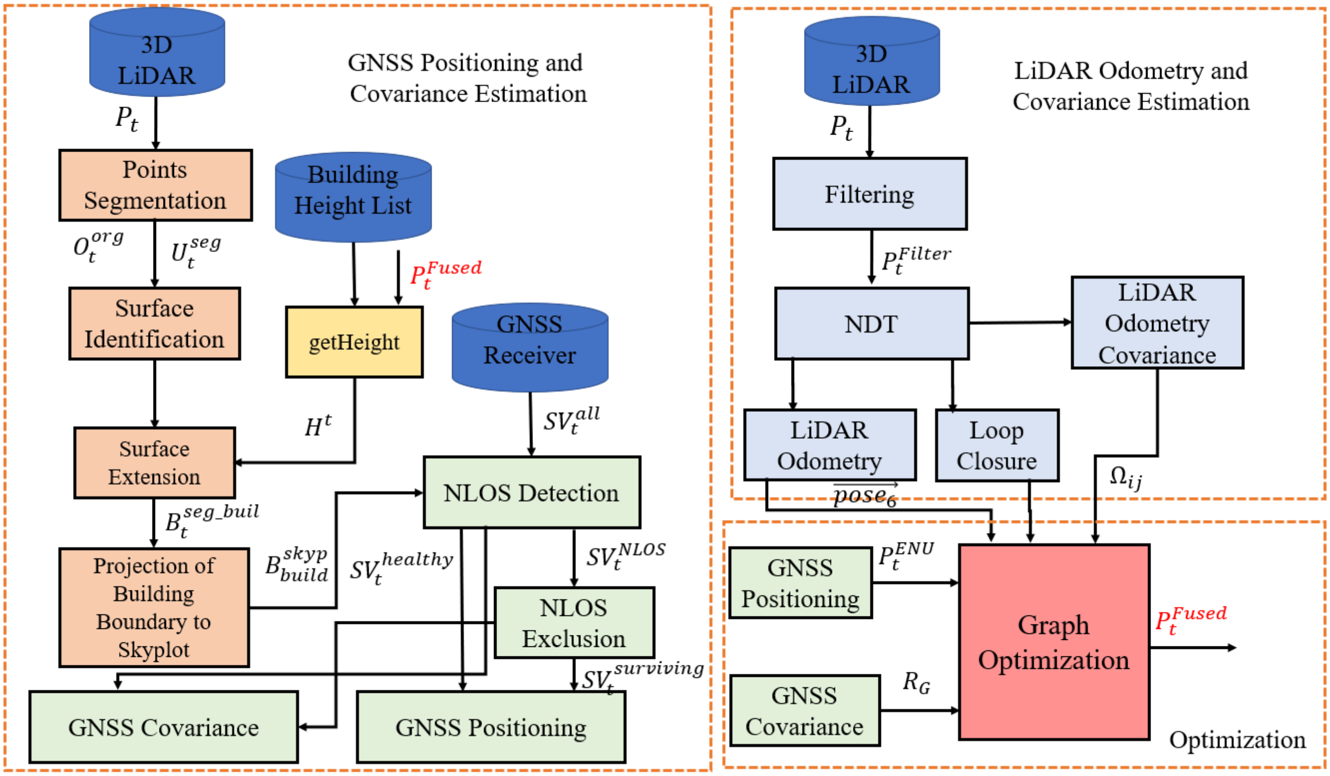

Fig. 3. The flowchart of the proposed GNSS/LiDAR integration method. Three parts are included: (a). GNSS positioning and its covariance estimation, (b). LiDAR odometry and its covariance estimation and (c). The graph-based optimization.

flowchart of the GNSS/LiDAR integration solution is shown in Fig. 3.

Firstly, the building boundary is detected based on the algorithm proposed in the previous work [43] of our research team. The point clouds are fixed to the GNSS frame based on the orientation obtained from LiDAR odometry (shown in Figure 3). The satellites and the building boundary are both projected to a GNSS Skyplot [44]. Secondly, the NLOS detection is conducted based on a proposed NLOS detection algorithm. GNSS measurements suffered from both NLOS, and low elevation angle is excluded based on a proposed FDE algorithm. Then, the GNSS positioning is conducted based on the survived GNSS measurements. Thirdly, the GNSS positioning covariance is calculated by considering the potential positioning errors caused by NLOS receptions and line-of-sight (LOS) receptions. Finally, the improved GNSS positioning result and corresponding covariance are integrated with the LiDAR odometry using a graph-based SLAM framework.

II. LIDAR ODOMETRY AND ITS COVARIANCE ESTIMATION

A. LiDAR Odometry

The principle of LiDAR odometry [45] is to track the transformation between two successive frames of point clouds by matching the two frames (called as a reference and an input point cloud in this paper). The matching process is also called point cloud registration. The objective of point cloud registration is to obtain the optimal transformation matrix to match or align the reference and the input point clouds. The most well-known method of point cloud registration is the iterative closest point (ICP) [46]. The ICP is a straightforward method to calculate the transformation matrix between two consecutive scans by iteratively searching pairs of nearby points in the two scans and minimizing the sum of all point-to-point distances. The objective function can be expressed as follows [46]:

$$C(\hat{\boldsymbol{R}},\hat{\boldsymbol{T}}) = \arg\min \sum_{i=1}^{N} ||(\boldsymbol{R}\boldsymbol{p}_i + \boldsymbol{T}) - \boldsymbol{q}_i||^2 \quad (1)$$

where the N indicates the number of points in one scan $\boldsymbol{p}$, $\boldsymbol{R}$ and $\boldsymbol{T}$ indicate the rotation and translation matrix, respectively, to transform the input point cloud ($\boldsymbol{p}$) into the reference point cloud ($\boldsymbol{q}$). Objective function $C(\hat{\boldsymbol{R}},\hat{\boldsymbol{T}})$ indicates the error of the transformation. The main drawback for this method is that ICP can easily get into the local minimum problem. The normal distribution transform [47] (NDT) is a state-of-art method to align two consecutive scans with modeling of points based on Gaussian distribution. The NDT innovatively divide the point clouds space into cells. Each cell is continuously modeled by a Gaussian distribution. In this case, the discrete point clouds are transformed into successive continuous functions. In this paper, the NDT is employed as the point cloud registration method for the LiDAR odometry. Assuming that the transformation between two consecutive frames of point clouds can be expressed as $\overrightarrow{\boldsymbol{pose}_6} = [t_x \quad t_y \quad t_z \quad \phi_x \quad \phi_y \quad \phi_z]^T$. The t_i indicates the translation in *x*, *y* and *z* axis, respectively. The ϕ_x

represents the orientation angle of the roll, pitch, and yaw, respectively. Steps of calculating the relative pose between the reference and the input point clouds are as follows:

1) Fetch all the points $\boldsymbol{x}_{i=1\ldots n}$ contained in a 3D cell [48]. Calculate the geometry mean $\boldsymbol{q} = \frac{1}{n}\sum_i \boldsymbol{x}_i$.
   Calculate the covariance matrix

$$\boldsymbol{\Sigma} = \frac{1}{n}\sum_i(\boldsymbol{x}_i - \boldsymbol{q})(\boldsymbol{x}_i - \boldsymbol{q})^T \tag{2}$$

2) The matching score is modeled as:

$$f(\boldsymbol{p}) = -\mathrm{score}(\boldsymbol{p}) = \sum_i \exp(-\frac{(\boldsymbol{x}_i{}' - \boldsymbol{q}_i)^T \boldsymbol{\Sigma}_i{}^{-1} (\boldsymbol{x}_i{}' - \boldsymbol{q}_i)}{2}) \tag{3}$$

   where $\boldsymbol{x}_i$ indicates the points in the current frame of scan $\boldsymbol{p}$. $\boldsymbol{x}_i{}'$ denotes the point in the previous scan mapped from the current frame using the $\overrightarrow{pose_6}$. $\boldsymbol{q}_i$ and $\boldsymbol{\Sigma}_i$ indicate the mean and the covariance of the corresponding normal distribution to point $\boldsymbol{x}_i{}'$ in the NDT of the previous scan.

3) Update the pose using the Quasi-Newton method based on the objective function to minimize the score, $\boldsymbol{f}(\boldsymbol{p})$.

With all the points in one frame of point clouds being modeled as cells, the objective of the optimization for NDT is to match current cells into the previous cells with the highest probability. The optimization function $f(\boldsymbol{p})$ can be found in [47]. In each cell containing several points, the corresponding covariance matrix can be calculated and represented by $\boldsymbol{\Sigma}$. The shape (circle, plane or linear) of the cell is indicated by the relations between the three eigenvalues of the covariance matrix [47]. In this case, comparing with the conventional ICP algorithm, the NDT innovatively optimize the transformation by considering the features of points. The loop closure detection is conducted based on these shape features [49].

B. *Covariance Estimation of LiDAR Odometry*

The LiDAR odometry can provide continuous relative pose estimation, $\overrightarrow{\boldsymbol{pose}_6}$. The associated covariance of this pose estimate is essential for the later integration with the GNSS positioning. During the NDT process, the covariance of pose estimation is related to the uncertainty of the matching between the reference and the input point clouds. In the graph-based optimization which will be introduced in Section IV, the covariance is indicated as the inverse of the information matrix $\boldsymbol{\Omega}_{ij}$. In each matching process between a point from the reference point cloud and a point from the input point cloud, we model the degree of matching as:

$$dm_{ij} = \frac{1}{n}\sum_{k=1}^{n}\sqrt{\Delta x_k^2 + \Delta y_k^2 + \Delta z_k^2} \tag{4}$$

where the dm_{ij} represent the degree of matching between the reference and the input point clouds. *n* represents the number of points in the input point cloud. Δx_k indicates the positional difference in *x*-axis between input and reference points after the convergence of NDT is obtained. Δy_k and Δz_k indicate the positional differences in *y* and *z* axis, respectively. Thus, the information matrix $\boldsymbol{\Omega}_{ij}$ of the degree of matching between reference and input can be expressed as:

$$\boldsymbol{\Omega}_{ij} = \begin{bmatrix} \boldsymbol{\Omega}_{ij}^p & 0 \\ 0 & \boldsymbol{\Omega}_{ij}^r \end{bmatrix} \tag{5}$$

$$\boldsymbol{\Omega}_{ij}^p = \boldsymbol{I}/(\mathrm{C}_p^2 dm_{ij}) \tag{6}$$

$$\boldsymbol{\Omega}_{ij}^r = \boldsymbol{I}/(\mathrm{C}_r^2 dm_{ij}) \tag{7}$$

where $\boldsymbol{I}$ indicates identity matrix, C_p^2 is a coefficient that is heuristically determined. In this case, the covariance for LiDAR odometry is correlated with the degree of matching. We can see from Fig. 2, the LiDAR matching can obtain relatively pose estimate on the lateral direction crossing the building. However, the longitudinal pose estimate is not as accurate as of the lateral one because the building surface tends to be plain and featureless. Thus, the covariance should be adaptively changed according to the degree of matching in different scenarios.

III. Object Detection Aided GNSS Positioning and Its Covariance Estimation

In this section, the detection of building boundary is presented firstly. The NLOS fault detection and exclusion (FDE) method is presented subsequently. Secondly, GNSS positioning is implemented based on the NLOS FDE. Finally, the innovative covariance estimation of GNSS positioning is introduced.

A. *Building Boundary Detection*

To identify which satellite is blocked by the surrounding buildings, the pose of the building boundaries relative to the GNSS receiver is needed. As the 3D LiDAR can provide sufficient points representing the environments, our previous work in [43] presents the detection of double-decker bus and dimensions extension algorithm based on LiDAR-based object detection. Building boundary detection is based on a similar approach. The process of building boundary detection is listed as follows:

1) Segment the point clouds into clusters to represent different objects.
2) Identify the building surface and extend the surface dimensions to the actual dimensions using Algorithm 1.
3) Obtain the bounding box indicating the building surface, and the corresponding top boundary.
4) Calculate the pose of the building relative to the GNSS receiver.

The inputs of Algorithm 1 are $\boldsymbol{U}_t^{seg}$ and $\boldsymbol{O}_t^{org}$ obtained from the segmentation based on the work in [43], point number threshold num_{thres}, length threshold len_{thres} and height threshold hei_{thres}, building height list $\boldsymbol{H}_{build}$, receiver position $\boldsymbol{P}_t^{fused}$, yaw angle $Yaw_r$from GNSS/LiDAR integration. The

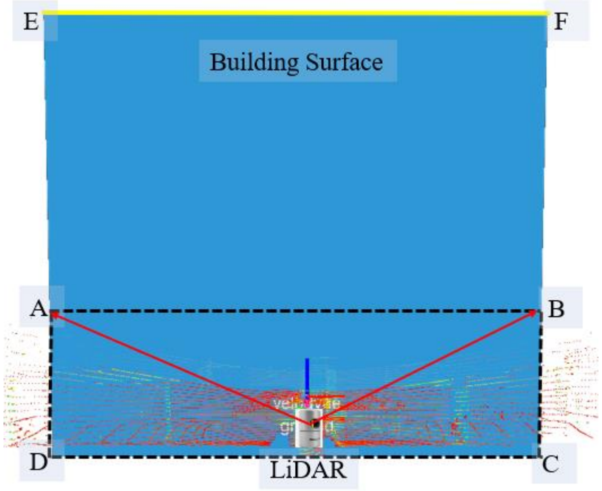

Fig. 4. Illustration of point sets segmentation and building surface identification. Blue box ABCD represents the initially detected building surface. Blue box CDEF represents the extended building surface.

output is the bounding box set $\boldsymbol{B}_t^{seg\_buil}$ specifically represent the building surface. Each bounding box is indicated by $\boldsymbol{U}_i = [x_i^c, y_i^c, z_i^c, roll_i^c, pitch_i^c, yaw_i^c, d_i^{len}, d_i^{wid}, d_i^{hei}]$. The function Num mentioned in Algorithm 1 is used to calculate the points number of each cluster $\boldsymbol{O}_i$. The function $getHeight$ is used to search the height information from a saved building height list containing the rough height information. To determine the actual height of the identified building surface, $\boldsymbol{P}_t^{fused}$, $\boldsymbol{U}_i$ and Yaw_r are also needed. $\boldsymbol{P}_t^{fused}$ indicates the GNSS position given by previous epoch positioning result from GNSS/LiDAR integration. The relative position between GNSS receiver and detected building can be obtained from $\boldsymbol{U}_i$. Moreover, the yaw angle can be acquired from GNSS/LiDAR integration. For each bounding box $\boldsymbol{B}_i$, the distance α_i from the receiver to the detected building surface can be calculated as follows:

$$\alpha_i = \sqrt{(x_i^{c\,2} + y_i^{c\,2} + z_i^{c\,2})} \tag{8}$$

Algorithm 1: Building surface identification from Bounding Box sets and height extension

Input: Bounding Box sets $\boldsymbol{U}_t^{seg} = \{\boldsymbol{U}_1, \boldsymbol{U}_2, \ldots, \boldsymbol{U}_i, \ldots \boldsymbol{U}_n, t\}$, Organized point clusters $\boldsymbol{O}_t^{org} = \{\boldsymbol{O}_1, \boldsymbol{O}_2, \ldots, \boldsymbol{O}_i, \ldots \boldsymbol{O}_n, t\}$, point number threshold num_{thres}, length threshold len_{thres} and height threshold hei_{thres}, building height list $\boldsymbol{H}_{build}$, receiver position $\boldsymbol{P}_t^{fused}$, yaw angle Yaw_r

Output: Bounding Box set represent building surfaces $\boldsymbol{B}_t^{seg\_buil} = \{\boldsymbol{B}_1, \boldsymbol{B}_2, \ldots, \boldsymbol{B}_i, \ldots \boldsymbol{B}_n, t\}$

```
set up an empty clusters list $\boldsymbol{B}_t^{seg\_buil}$ to save bounding box
for all bounding box $\boldsymbol{U}_i$ in $\boldsymbol{U}_t^{seg}$ do
  if Num$(O_i) > num_{thres}$
    $\boldsymbol{U}_i \leftarrow [x_i^c, y_i^c, z_i^c, roll_i^c, pitch_i^c, yaw_i^c, d_i^{len}, d_i^{wid}, d_i^{hei}]$
    if $d_i^{len} > len_{thres}$ and $d_i^{hei} > hei_{thres}$
      $d_i^{hei} \leftarrow getHeight(\boldsymbol{H}_{build}, \boldsymbol{P}_t^{fused}, \boldsymbol{U}_i, Yaw_r)$
      $\boldsymbol{B}_i \leftarrow \boldsymbol{U}_i$
    end if
  end if
end for $\boldsymbol{U}_t^{seg}$
```

Thus, the bounding box with extended height representing the building surface can be identified using Algorithm 1. The bounding box is extended from rectangles ABCD to CDEF as can be seen in Fig. 4. The bounding boxes ABCD and CDEF indicate the initially detected dimensions and the extended dimensions of the building, respectively. Then, the boundary parameters for the bounding box $\boldsymbol{B}_i$ corresponding to building surface is denoted by the line segment $\overline{EF}$ denoted as $\boldsymbol{B}_{build}^{3d}$, the matrix of bus boundary. To represent the building, two points, E and F, are required. The $\boldsymbol{B}_{build}^{3d}$, which is relative to the LiDAR coordinate system, is structured as follows:

$$\boldsymbol{B}_{build}^{3d} = \begin{bmatrix} x_{3dE} & y_{3dE} & z_{3dE} \\ x_{3dF} & y_{3dF} & z_{3dF} \end{bmatrix} \tag{9}$$

In this case, the top boundary of the building is detected which is used for NLOS detection in the following sub-section. The distance between the receiver and the building surface is calculated as α_i which will be used for the covariance estimation of GNSS positioning in Section III-D.

B. NLOS Detection and Exclusion

The boundary of the building is detected as $\boldsymbol{B}_{build}^{3d}$. The satellites and the building boundary can be projected into a GNSS Skyplot which is shown in Fig. 5. The circles indicate the satellites and the associated number represents the satellite index. The yellow line indicates the building boundary projected into the Skyplot. The NLOS is indicated with a red circle in Fig. 5. Assume that the initial satellites set are $\boldsymbol{SV}_t^{all} = \{\boldsymbol{SV}_1, \boldsymbol{SV}_2, \ldots, \boldsymbol{SV}_i, \ldots \boldsymbol{SV}_s\}$, where $\boldsymbol{SV}_i = \{az_i, el_i, SNR_i, \rho_i\}$. az_i and el_i denote the azimuth and elevation angles of a satellite, respectively, SNR_i indicates satellite SNR and ρ_i denotes the pseudorange measurement. The satellite visibility classification based on satellite information and boundaries is introduced in the previous work [50] of our research team. According to Fig. 5, we can have two satellite sets. One is the satellites set $\boldsymbol{SV}_t^{nlos} = \{\boldsymbol{SV}_1, \boldsymbol{SV}_2, \ldots, \boldsymbol{SV}_i, \ldots \boldsymbol{SV}_n\}$ containing only the NLOS ones. The other one is the LOS satellite set $\boldsymbol{SV}_t^{los} = \{\boldsymbol{SV}_1, \boldsymbol{SV}_2, \ldots, \boldsymbol{SV}_i, \ldots \boldsymbol{SV}_l\}$ and $s = n + l$ is satisfied.

We can see from the Skyplot in Fig. 5, the majority of the satellites are blocked (6 blocked out of 12 satellites). Almost only satellites with elevation angle more than 72 degrees are not blocked. The exclusion of all the NLOS receptions can result in a significant increase in the HDOP which will magnify the pseudorange errors in GNSS positioning. In other words, fully exclusion of NLOS receptions will conversely deteriorate the GNSS positioning result. In the previous work, we analyze NLOS errors in [27]. The pseudorange error is smaller while

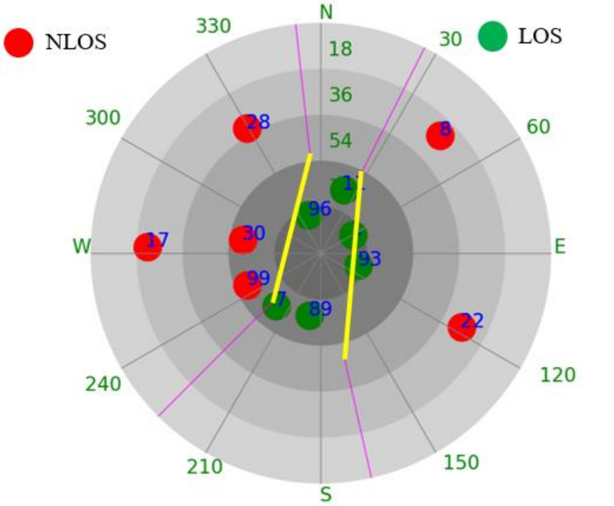

Fig. 5. GNSS Skyplot indicates the satellites distribution and building boundary.

the higher of elevation angle and smaller the distance from GNSS receiver to the reflector (refers to α_i shown in Fig.2). In other words, the NLOS with lower elevation angle can introduce larger GNSS positioning error. The relations between the satellite elevation, α_i and pseudorange error are presented in [27].

Inspired by this result [51], this paper proposes to exclude the measurement based on satellite elevation angle and the HDOP of satellites distribution. The proposed satellites exclusion method is shown in Algorithm 2. The inputs of the algorithm include the NLOS satellites information sets $\boldsymbol{SV}_t^{nlos} = \{\boldsymbol{SV}_1, \boldsymbol{SV}_2, \dots, \boldsymbol{SV}_i, \dots \boldsymbol{SV}_n\}$ and $\boldsymbol{SV}_t^{los}$. Only the satellites blocked by buildings are contained in the satellite set $\boldsymbol{SV}_t^{nlos}$ (for example, the satellite 8, 17, 28, 22, 30, 39 shown in Fig. 5). The thresholds for elevation angle and HDOP are also the inputs of Algorithm 2. The output of Algorithm 2 is the satellites set survived from this NLOS exclusion process, indicated as $\boldsymbol{SV}_t^{los\_nlos} = \{\boldsymbol{SV}_1^s, \boldsymbol{SV}_2^s, \dots, \boldsymbol{SV}_i^s, \dots \boldsymbol{SV}_m^s\}$.

After the proposed NLOS exclusion, part of the NLOS measurements is excluded with low elevation angles. The survived NLOS and LOS measurements are saved into the $\boldsymbol{SV}_t^{los\_nlos}$. This satellite set is used for GNSS positioning using WLS method in the following sub-section.

Algorithm 2: Proposed NLOS Exclusion

```
Input: Satellites information set $\boldsymbol{SV}_t^{nlos} = \{\boldsymbol{SV}_1, \boldsymbol{SV}_2, \dots, \boldsymbol{SV}_i, \dots \boldsymbol{SV}_n\}$, $\boldsymbol{SV}_t^{los} = \{\boldsymbol{SV}_1, \boldsymbol{SV}_2, \dots, \boldsymbol{SV}_i, \dots \boldsymbol{SV}_l\}$ ,elevation angle threshold $el_{threshold}$, threshold of HDOP $H_{thres}$
Output: corrected satellites set after NLOS exclusion: $\boldsymbol{SV}_t^{los\_nlos} = \{\boldsymbol{SV}_1^s, \boldsymbol{SV}_2^s, \dots, \boldsymbol{SV}_i^s, \dots \boldsymbol{SV}_m^s\}$
Step 1: sort the satellites set in $\boldsymbol{SV}_t^{nlos}$ based on
        elevation angle from small to large
Step 2: exclude satellite $\boldsymbol{SV}_i$ from $\boldsymbol{SV}_t^{nlos}$ if:
    • its elevation angle is smaller than $el_{threshold}$
    • The HDOP of the remaining satellites (including the remaining satellites in $\boldsymbol{SV}_t^{nlos}$ and satellites in $\boldsymbol{SV}_t^{los}$) is smaller than the HDOP threshold $H_{thres}$.
Step 3: repeat step 2 until all the conditions in step 2
        cannot be fully satisfied.
Step 4: save the remaining satellites in $\boldsymbol{SV}_t^{nlos}$ and
        $\boldsymbol{SV}_t^{los}$to $\boldsymbol{SV}_t^{los\_nlos} = \{\boldsymbol{SV}_t^{nlos},\ \boldsymbol{SV}_t^{los}\}$.
```

C. *GNSS Weight Least Square Positioning*

Satellites in $\boldsymbol{SV}_t^{los\_nlos}$ are employed for GNSS positioning calculation. The system clock bias between the GNSS receiver and satellites is contained in the pseudorange measurements. The equation linking the receiver position and range measurements can be structured as the following least square (LS) method:

$$\hat{\boldsymbol{x}} = (\boldsymbol{G}^T\boldsymbol{G})^{-1}\boldsymbol{G}^T\boldsymbol{\rho} \tag{10}$$

where $\boldsymbol{G}$ represents the observation matrix and is structured by unit LOS vectors between the GNSS receiver's position and satellite's position. $\hat{\boldsymbol{x}}$ indicates the estimated receiver position and $\boldsymbol{\rho}$ denotes the pseudorange measurements.

Conventionally, to better represent the reliability of each measurement based on the information measured by the receiver, weightings of each measurement are needed. Function to calculate the weighting by integrating the measurement SNR and satellite elevation angle is expressed as $\boldsymbol{W}$ [52]. Finally, the GNSS receiver position can be estimated using the WLS method as:

$$\hat{x} = (\boldsymbol{G}^T\boldsymbol{W}\boldsymbol{G})^{-1}\boldsymbol{G}^T\boldsymbol{W}\boldsymbol{\rho} \tag{11}$$

In this paper, the GNSS positioning result is represented as $\boldsymbol{P}_t^{ENU} = [x_E \quad y_N \quad z_u]$ in the ENU coordinate system [53].

D. *GNSS Positioning Covariance Estimation*

Conventionally, the GNSS uncertainty is usually modeled by considering the SNR, satellites numbers and HDOP if the NLOS satellites are not identified [40]. This rough modeling can only work in open-sky environments with little NLOS receptions. The team in the University of Illinois [42] propose to model the GNSS positioning uncertainty solely based on the SNR [42] after identifying and excluding the NLOS receptions. However, fully NLOS exclusion is not acceptable in the super-urbanized area as it can result in a significant increase in HDOP. In this paper, we propose to model the covariance matrix of GNSS positioning that consisted of two parts, the NLOS and LOS, as following:

$$\boldsymbol{R}_G = \boldsymbol{R}_C + \boldsymbol{R}_E \tag{12}$$

The $\boldsymbol{R}_C$ is the covariance matrix indicates the uncertainty of GNSS positioning with the assumption that all the satellites used for positioning in $\boldsymbol{SV}_t^{los\_nlos}$ are line-of-sight. The $\boldsymbol{R}_C$ is calculated as follows:

$$\boldsymbol{R}_C = \begin{pmatrix}1 & 0\\ 0 & 1\end{pmatrix} HDOP_{xy}\sigma_{UERE}^2 \tag{13}$$

σ_{UERE} indicates the user-equivalent range error (UERE) and is experimentally determined in this paper. The $HDOP_{xy}$ is the HDOP of the GNSS positioning.

The $\boldsymbol{R}_E$ is the covariance matrix indicates the extra uncertainty of GNSS positioning caused by the NLOS. The $\boldsymbol{R}_E$ is calculated as follows:

$$\boldsymbol{R}_E = \begin{pmatrix}1 & 0\\ 0 & 1\end{pmatrix} HDOP_{xy}\sigma_{NLOS}^2 \tag{14}$$

σ_{NLOS} indicates the extra uncertainty caused by the NLOS receptions. According to [27], the pseudorange error for each NLOS measurement can roughly be modeled as follows:

$$\gamma = \alpha(sec\theta_{elc}(1 + cos2\theta_{elc}) + sec\theta_{azm}(1 + cos2\theta_{azm})) \tag{15}$$

where α represent the distance between the GNSS receiver and the reflector and is obtained from the surface detection presented in Section III-A. The θ_{elc} and θ_{azm} represents the elevation and azimuth angles, respectively. Thus, we can obtain the total uncertainty of pseudorange σ_{NLOS} for all the satellites (totally k satellites) as following:

$$\sigma_{NLOS} = \sum_{i=1}^{k} \gamma_i \tag{16}$$

In this case, the covariance of GNSS positioning is calculated by considering both the LOS and the NLOS measurement. The component needed to be estimated in the matrix $\boldsymbol{R}_G$ is the following:

$$\overline{\boldsymbol{R}} = HDOP_{xy}\sigma_{NLOS}^2 + HDOP_{xy}\sigma_{UERE}^2 \tag{17}$$

Moreover, only the covariance in the horizontal direction is obtained. In the super-urbanized area, the vertical dilution of precision (VDOP) is significantly larger than the HDOP. The positioning error in the vertical direction can be very bad due to the distorted vertical distribution of the satellites. Thus, only the horizontal GNSS positioning and the corresponding covariance are used in the proposed GNSS/LiDAR integration.

IV. Graph-based GNSS/LiDAR integration

This section presents the graph-based GNSS/LiDAR integration. Pose graph optimization is to construct all the measurements into a graph as constraints and calculate the best set of poses by solving a non-linear optimization problem. In this paper, the constraints are provided by both the object detection aided GNSS positioning and the LiDAR odometry. Two steps are needed to implement the graph-based GNSS/LiDAR integration optimization, the graph generation, and graph optimization.

A. Graph Generation

The graph is constituted by edges and vertexes [26]. Edges are provided by the observation measurements including the GNSS and the LiDAR as shown in Fig. 6. The $\boldsymbol{x}_i$ represents the 6-dimension (6D) pose estimation that included the position and orientation. $\boldsymbol{e}_{ij}$ indicates the error function evaluating the difference between the estimated state and the observation from sensors. $\boldsymbol{z}_{ij}$ represents the observation. In the graph optimization, the $\boldsymbol{x}_i$ is the state. The observations include three parts, the measurements from the GNSS, loop closure, and the LiDAR positioning presented in Sections II and III, respectively. The blue circles and red lines represent the nodes and the edges respectively, which are provided by the globally referenced GNSS positioning. The red circles and blue lines indicate the nodes and the edges respectively, provided by LiDAR odometry. The black line indicates the edge provided by loop closure. The error function for GNSS observation is expressed as follows:

$$\boldsymbol{e}_i^{GNSS} = ||h_i(\boldsymbol{x}_i) - \boldsymbol{z}_i^{GNSS}||_{\boldsymbol{\Omega}}^2 \tag{18}$$

where the $h_i(*)$ is the measurement function, relating between the GNSS measurement $\boldsymbol{z}_i^{GNSS}$ to the state $\boldsymbol{x}_i$. $\boldsymbol{\Omega}$ is the covariance matrix of the corresponding observation measurement.

LiDAR odometry can provide continuous 6D pose estimate and corresponding covariance. The error function for LiDAR odometry is expressed as:

$$\boldsymbol{e}_i^{LiDAR} = ||\boldsymbol{x}_i - \boldsymbol{x}_{i-1} - \boldsymbol{z}_i^{LiDAR}||_{\boldsymbol{\Omega}}^2 \tag{19}$$

where the $\boldsymbol{z}_i^{LiDAR}$ is the measurement from LiDAR odometry. Loop closure can be detected when the vehicle passes similar or neighboring area again. The error function for loop closure is expressed as:

$$\boldsymbol{e}_{i,j}^{loop} = ||\boldsymbol{x}_i - \boldsymbol{x}_j - \boldsymbol{z}_i^{loop}||_{\boldsymbol{\Omega}}^2 \tag{20}$$

where the $\boldsymbol{z}_i^{loop}$ is the measurement from loop closure.

Only 2D horizontal positioning and corresponding covariance are provided by GNSS positioning in this paper. GNSS positioning error can go up to ~50 meters in super-urbanized area. As the covariance of GNSS positioning is reasonably estimated by considering the NLOS and LOS receptions, we propose to add the GNSS results into the graph (shown in Fig. 6) only when the $\sqrt{\overline{\boldsymbol{R}}}$ of GNSS positioning is smaller than a

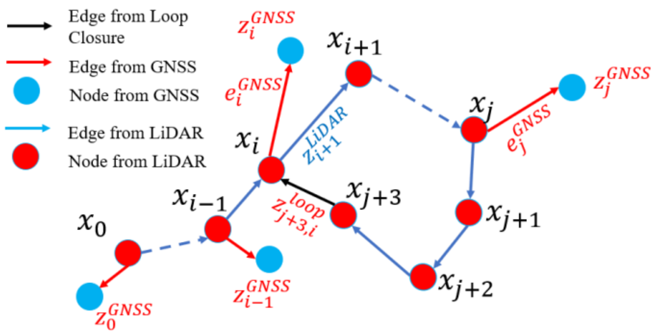

Fig. 6. A demonstration of graph generation based on GNSS and LiDAR positioning.

threshold $\boldsymbol{R}_{threshold}$. In this case, only the GNSS measurement with small covariance is applied to the graph optimization for providing the globally referenced update. This exclusion can prevent the severely biased GNSS positioning result being applied to the graph. The detail of graph generation is shown in Algorithm 3.

Algorithm 3: Proposed Graph Generation

```
Input: GNSS results $\boldsymbol{z}_i^{GNSS}$ and the corresponding covariance $\overline{\boldsymbol{R}}_i$. LiDAR odometry observation $\boldsymbol{z}_i^{LiDAR}$, loop closure $\boldsymbol{z}_i^{loop}$
Output: Graph of nodes and vertexes
Step 1: Initialize the estimated state using the GNSS
        results.
Step 2: Add the observation $\boldsymbol{z}_i^{LiDAR}$ from LiDAR
        odometry into the graph if any of the
        following conditions are satisfied:
            • The translation between the current
              LiDAR odometry and the previous node
              in the graph overweigh $Tran_{threshold}$.
            • The rotation between the current LiDAR
              odometry and the previous node in the
              graph overweigh $Rot_{threshold}$.
Step 3: Add the observation of GNSS results in the
        graph if:
            • The value $\sqrt{\overline{\boldsymbol{R}}_i}$ is smaller than $\boldsymbol{R}_{threshold}$.
Step 4: Add the observation $\boldsymbol{z}_i^{loop}$ from loop closure
        into the graph if loop closure is detected.
Step 5: Repeat Steps 2 and 3 until the end.
```

Comparing with the conventional graph-based GNSS/LiDAR integration, this paper innovatively adds the improved GNSS results and corresponding covariance into the graph optimization. The effectiveness of this novelty is subjected to the performance of the uncertainty estimation of GNSS positioning which is introduced in Section III-D.

B. Graph Optimization

The graph optimization [54] is straightforward that took all the constraints into a non-linear optimization problem. The optimization form is shown as following:

$$F(\mathrm{x}) = \sum_{i,j} ||h_i(\boldsymbol{x}_i) - \boldsymbol{z}_i^{GNSS}||_{\boldsymbol{\Omega}}^2 + ||\boldsymbol{x}_i - \boldsymbol{x}_{i-1} - \boldsymbol{z}_i^{LiDAR}||_{\boldsymbol{\Omega}}^2 + ||\boldsymbol{x}_i - \boldsymbol{x}_j - \boldsymbol{z}_i^{loop}||_{\boldsymbol{\Omega}}^2 \quad (21)$$

where $F(x)$ is the optimization function which is the sum errors of all the edges. $\boldsymbol{\Omega}_{ij}$ is the information matrix indicating the importance of each constraint in the global graph optimization. The information matrix is the inverse of the covariance matrix. The final solution to this optimization is the $\boldsymbol{x}^*$ (6D pose estimate) satisfying the following function:

$$\boldsymbol{x}^* = argminF(\boldsymbol{x}) \quad (22)$$

Thus, the optimization lies in solving the equation above to obtain the optimal $\boldsymbol{x}^*$. We can see from the optimization form $F(\boldsymbol{x})$, the covariance of the GNSS and LiDAR odometry positioning results are reflected in $\boldsymbol{\Omega}$. If the covariance of each positioning result is not properly estimated, the global optimization will be deflected resulting in the erroneous final pose sets.

V. Experimental Evaluation

To evaluate the performance of the proposed GNSS/LiDAR integration method in this paper, two experiments are presented in this section. The performance of LiDAR stand-alone positioning in diverse urban scenarios is extensively evaluated in previous work [55] of our research team.

GNSS positioning results are presented at first. Then, the GNSS/LiDAR integration experiment results are analyzed.

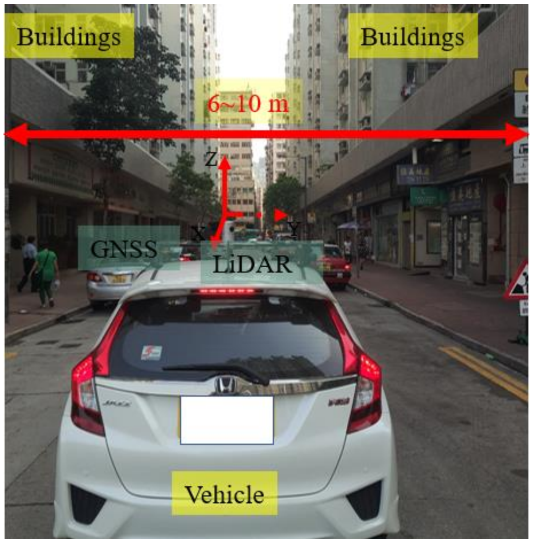

Fig. 7. The sensors setup of the vehicle: GNSS and LiDAR sensors are installed on the top of the vehicle.

A. Experimental Setup

Two experiments are conducted in Hong Kong. The first experiment is implemented in a narrow street with buildings on both sides which can be seen in Fig. 7. Both sides of the road are filled with buildings and the distance between the buildings is just 7~10 meters (see in Fig. 7). The experiment is conducted with an open loop route. The other experiment is conducted with a closed loop route, and loop closure is available for the GNSS/LiDAR integration. The objective of this closed drive is to validate that the proposed GNSS/LiDAR integration solution

TABLE I
PERFORMANCE OF THE THREE GNSS POSITIONING METHODS (2D POSITIONING)

All data	**Conventional: WLS**	**WLS-NE-A (Excluding all NLOS)**	**WLS-NE-P (Partially Excluding NLOS)**
Mean Error	29.81 m	30.25 m	**27.09 m**
std	21.09 m	22.28 m	19.6 m
Availability	100%	97.45%	100%

is repeatable in diverse scenarios and the overall performance can be well enhanced with the aid of loop closure.

In both of the experiments, the u-blox M8T receiver is used to collect raw GPS and BeiDou measurements. 3D LiDAR sensor, Velodyne 32, is employed to provide the real-time point clouds scanned from the surroundings. Both u-blox receiver and 3D LiDAR are installed on the top of a vehicle during the experiment which can be seen in Fig. 7. The data were collected within approximately 5 minutes' drive at a frequency of 1 Hz for GNSS and 10 Hz for 3D LiDAR using Robot Operation System (ROS) [56] time to synchronize all the sensor information. The sensor setup and the corresponding coordinate system are shown in Fig. 7 with *x*-axis (LiDAR coordinate system) pointing back of the vehicle. The GNSS positioning is represented in ENU reference system. The initial position of the experiment is employed as the initial position calculation of ENU coordinates. Moreover, LiDAR coordinate is shown in Figure 7 and are calibrated [55] with GNSS in ENU [57] coordinate at the beginning of the experiment.

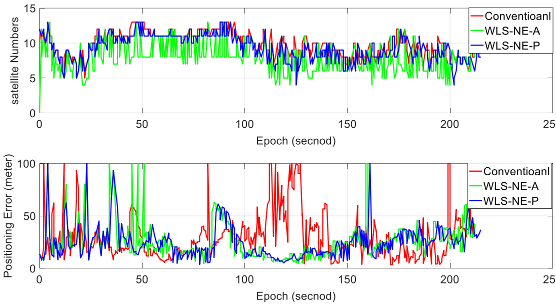

Fig. 8. Experiment 1: Experimental results of WLS and WLS-NE, which depicted in red and blue dots, respectively. Top panel indicates the numbers of satellites used. Bottom panels indicates the 3D positioning errors.

In addition, the NovAtel SPAN-CPT, GNSS/INS (fiber optic gyroscopes) integrated navigation system is used to provide the ground truth trajectory with decimeter level accuracy.

B. Experimental Evaluation using Data Collected by Open Loop Route

1) GNSS Positioning Evaluation

GNSS positioning is evaluated by comparing WLS-based GNSS positioning with the GNSS positioning aided by NLOS exclusion. The result of the GNSS positioning (2 dimensions) using different methods are listed in TABLE I. If all the NLOS receptions are excluded from GNSS positioning, the result is shown in the third column. The result obtained by the proposed NLOS exclusion method in Algorithm 2 (WLS-NE) is shown in the fourth column. Due to the blockage from the tall buildings, the majority of the measurements are NLOS.

The conventional WLS method can obtain 29.81 meters of mean error. The error magnitude is much larger than the positioning error in [36] where its experiment is conducted in less urbanized areas. The standard deviation is 21.09 and the availability is 100% during the test. With the exclusion of all the NLOS measurements, the GNSS positioning is even worse. The mean of its positioning error goes up to 30.25 meters and the standard deviation also slightly increase. Moreover, the availability of this solution decreases to 97.45 %. This result shows that the exclusion of all NLOS measurements may not improve the overall performance in highly urbanized areas. This is due to the distortion of the satellite's geometric distribution, namely, larger HDOP occurs.

With the proposed method shown in Algorithm 2, the mean positioning error is slightly improved from 29.81 to 27.09 meters. Moreover, the availability of the GNSS solution is guaranteed (100%). The improvement is not too large because of the excessive NLOS receptions in the tested scenario.

The satellite numbers and the GNSS positioning results are shown in Fig. 8. The green curve represents the number of the satellite when all the NLOS receptions are excluded. The blue curve indicates the satellite number based on the proposed NLOS exclusion algorithm (Algorithm 2). The satellite number can be decreased to less than 5 if all the NLOS receptions are excluded which can be seen in the top panel of Fig. 8. Due to the frequent NLOS exclusion based on Algorithm 2, the satellite number is slightly decreased comparing to the red curve. Only part of the identified NLOS is excluded using Algorithm 2 can guarantee enough satellites for GNSS positioning calculation. As shown in the bottom panel of Fig. 8, the proposed NLOS exclusion can introduce improvements sometimes instead of all the time. This is because there are too

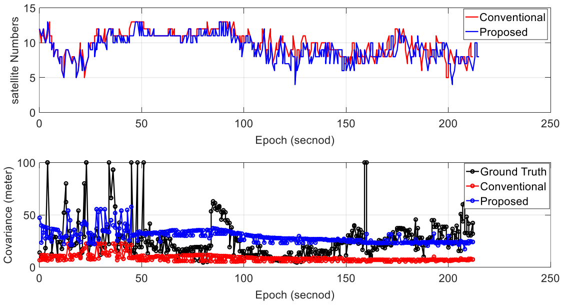

Fig. 9. Experiment 1: Top panel indicate the numbers of satellite used in the conventional and proposed GNSS positioning methods. Bottom panel indicates the corresponding covariance estimated. The conventional and proposed covariance estimation are indicated in red and blue dots, respectively. GNSS positioning error using the WLS-NE is represented in black dots (ground truth for covariance).

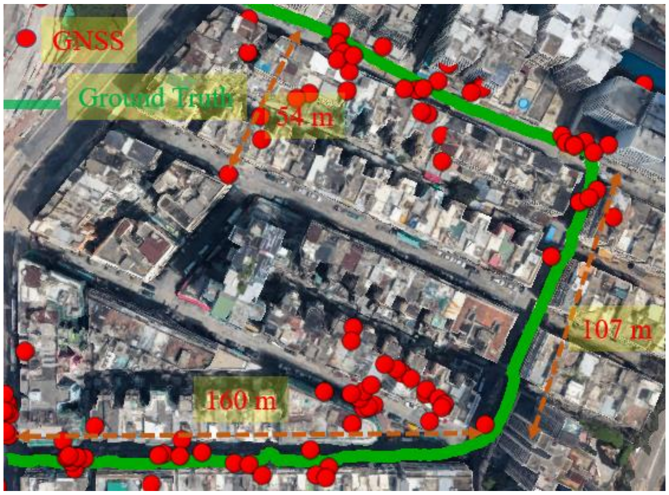

Fig. 10. Experiment 1: Trajectory of the autonomous vehicle is indicated by green curve. The red circles indicate the GNSS positioning result.

many NLOS receptions and exclusion can also enlarge the HDOP in some ways.

The result of covariance estimation based on the proposed method in Section III-D is shown in Fig. 9. The black dots represent the GNSS positioning error using the WLS-NE method. This is the value that the estimated covariance expected to approach. The red dots represent the conventional GNSS covariance estimation based on the method in [41] ($\boldsymbol{R}_C$). This method cannot model the NLOS error caused by signal reflection. We can see from the Fig. 9, this covariance estimation slightly fluctuated due to the change in HDOP. However, this covariance is far from the black dots. The blue dots represent the proposed GNSS positioning covariance estimation result based on $\sqrt{\overline{\boldsymbol{R}}}$ as shown in (17). This covariance is closer to the black dots (refer to the ground truth of covariance) comparing with that of the conventional covariance. As shown in Fig. 9, the proposed covariance can effectively model the GNSS positioning error in some epochs, especially when then GNSS positioning error is smaller. However, some epochs encounter a large difference between the estimated covariance and actual positioning error. This is because the proposed method can only identify the NLOS near the vehicle which is within the detection range of the 3D LiDAR (commonly 120 meters). The NLOS that its reflector too far away from the vehicle is not be modeled by the proposed covariance estimation method. Moreover, the multipath effects are also not modeled in this covariance estimation method.

TABLE II
EXPERIMENT 1: PERFORMANCE OF THE THREE GNSS/LIDAR INTEGRATION METHOD

All data	Method (a) Conventional GNSS/LiDAR Integration	Method (b) Proposed GNSS/LiDAR Integration	Method (c) Proposed GNSS/LiDAR Integration B
Mean Error	24.07 m	22.67 m	12.67 m
STD	14.69 m	14.48 m	6.57 m
Availability	100%	100%	100%

2) GNSS/LiDAR Integration Evaluation

The trajectory of the tested vehicle is shown in Fig. 10. The red circles represent the GNSS positioning results using the proposed WLS-NE method. The green curve indicates the ground truth of the tested trajectory. We can see from the figure that the majority of the epochs possess large positioning error. In the GNSS/LiDAR integration, GNSS is the only source that can provide absolute positioning information. The graph generation in the SLAM is shown in Fig. 11. Fig. 11 indicates the organized point cloud, nodes and edges for further graph-based optimization.

As we can see from Fig. 8, the WLS-NE based GNSS positioning solution can still even reach 54 meters. In this section, three GNSS/LiDAR integration methods are compared.

- Method (a): GNSS/LiDAR integration with conventional GNSS covariance estimation [41].
- Method (b): GNSS/LiDAR integration with proposed GNSS covariance estimation.
- Method (c) GNSS/LiDAR integration with proposed GNSS covariance estimation. However, GNSS positioning is integrated into graph optimization only when $\sqrt{\overline{\boldsymbol{R}}}$ is smaller than the threshold$R_{threshold}$.

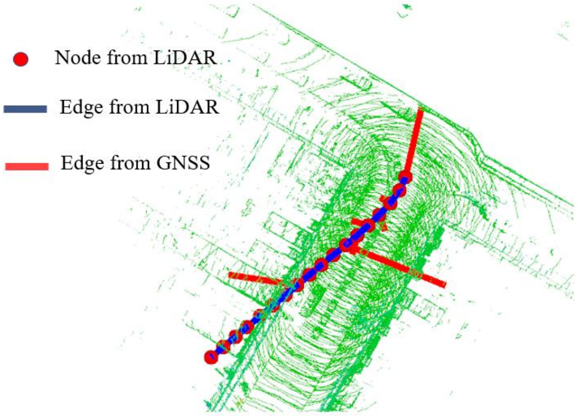

Fig. 11. Graph generation in the real graph-slam process.

The GNSS/LiDAR integration results are given in Table II using the three methods. The mean error of the conventional GNSS/LiDAR integration is 24.07 meters and is improved comparing with the performance of GNSS standalone (27.09 meters). With the aid of proposed GNSS positioning covariance (Method (b)), the error of GNSS/LiDAR integration is slightly decreased to 22.67 meters. The standard deviation is also slightly decreased. In the integration method (b), all the GNSS positioning results and corresponding covariance are applied in the GNSS/LIDAR integration. As the majority of the GNSS positioning is erroneous, it is reasonable to use GNSS results when it is accurate. The accurate results can be identified when its estimated covariance is less than $R_{threshold}$. Dramatic improvement is obtained after the constraint of covariance is applied. The mean error and standard deviation are decreased to 12.67 and 6.57 meters, respectively. Moreover, the availabilities of all three methods are 100%. This improvement shows that the proposed covariance estimation can improve the performance of the GNSS/LiDAR integration. The GNSS/LiDAR integration results are shown in Fig. 12. Comparing to the Bayes filter-based [13, 14] sensor fusion method, the graph-based GNSS/LiDAR integration takes all the constraints into the optimization framework. Thus, the poses of the whole organized point clouds, nodes, edges changed over time. We can see from Fig. 12 and conclude that:

(1) The proposed method (c) obtained the most accurate trajectory over the three methods.

(2) The positioning error decreased near the end of the drive, meaning that the GNSS/LiDAR integration can mitigate the drift of LiDAR odometry.

The error of GNSS/LiDAR integration is shown in Fig. 13. We can see from the figure that the method (c) outperforms the other two methods over the majority of the epochs.

The previous research [10, 40] tends to integrate the GNSS and LiDAR in the scenario where the GNSS positioning error is less than 5~8 meters using GNSS WLS. In this tested scenario, the GNSS results with an enormous error are applied in the GNSS/LiDAR integration which is very common in super-urbanized cities such as Hong Kong.

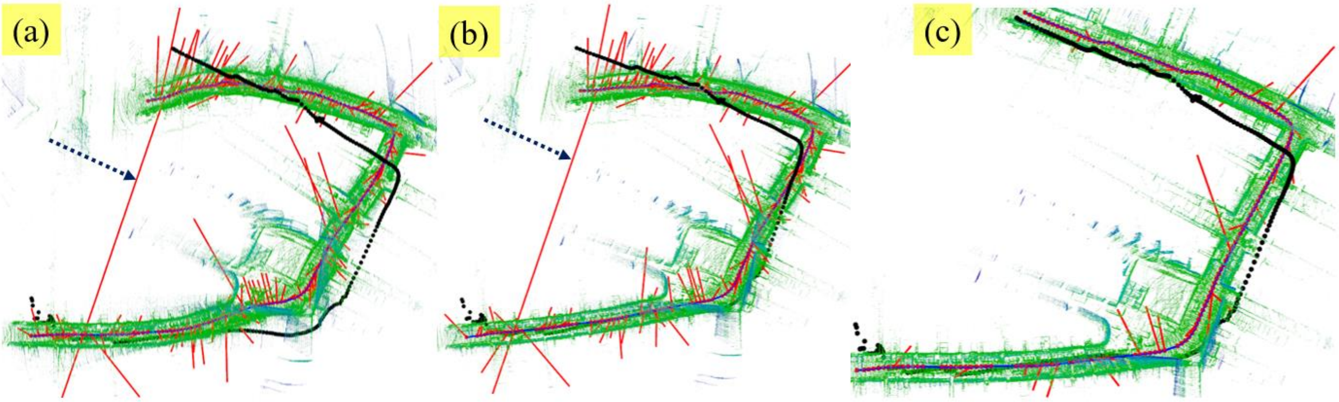

Fig. 12. Experiment 1: Results of the GNSS/LiDAR integration based on three integration methods. The blue curve is constituted by the optimized nodes (refer to the red node in Fig. 6. The black curve indicates the ground truth of the trajectory that provided by NovAtel SPAN-CPT. The red line represents the edge from GNSS positioning: refer to the red line in Fig. 6). The green points represent the organized point clouds.

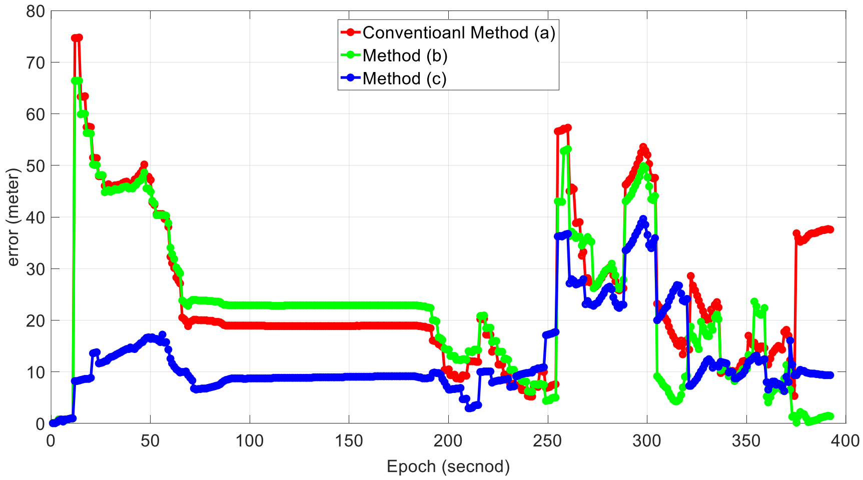

Fig. 13. Experiment 1: Positioning error of the GNSS/LiDAR integration results based on the three methods. Red, green and blue curves indicate the GNSS/LiDAR integration methods (a), (b) and (c), respectively.

C. *Experimental Evaluation using Data Collected by Closed Loop Route*

1) *GNSS Positioning Evaluation*

This experiment is conducted in a super-urbanized area with fewer satellites visible comparing with that of the first

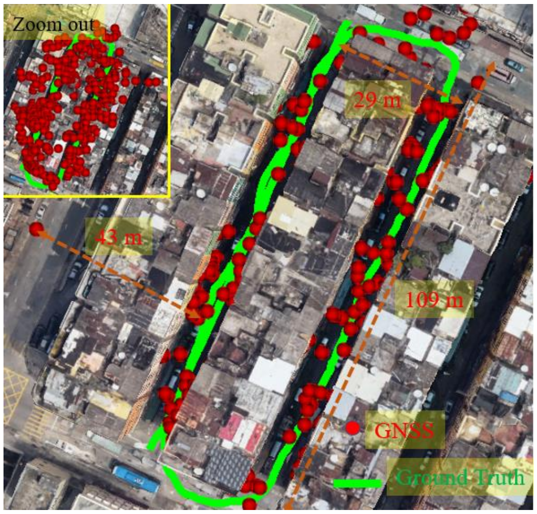

Fig. 14. Experiment 2: Trajectory of the vehicle is indicated by green curve. The red circles indicate the object detection aided GNSS positioning results.

experiment. Moreover, this experiment route is a closed loop. The loop closure [49] detection is employed in the GNSS/LiDAR integration process in this experiment. The experiment scene is shown in Fig. 14. The height of the building is about 30 meters. The distance between the buildings is just about 8 meters. We can see from the figure that the majority of the GNSS positioning results lie into the buildings due to the multipath effects and the excessive NLOS receptions. Again, the mean error is slightly reduced from 46.62 (conventional WLS) meters to 43.12 meters (proposed WLS-NE).

The covariance estimation result of the proposed method is shown in Fig. 15. Compared with the covariance estimation in the first experiment shown in Fig. 9, the covariance is better estimated in this experiment. The main reason is that the majority of the satellites are NLOS due to the tall building which means less multipath effects. As discussed earlier, the multipath is not modeled in the proposed covariance estimation method. In other words, the proposed GNSS positioning covariance estimation method can obtain better performance in narrower streets.

2) *GNSS/LiDAR Integration Evaluation*

GNSS/LiDAR integration performance is shown in TABLE III. The loop closure detection is applied in this experiment as the driving route is a closed loop shown in Fig. 14.

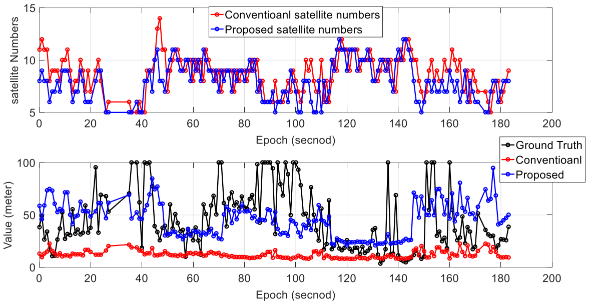

Fig. 15. Experiment 2: Top panel indicate the numbers of satellite used in the conventional and proposed GNSS positioning methods. Bottom panel indicates the corresponding covariance estimated. The conventional and proposed covariance estimation are indicated in red and blue dots, respectively. GNSS positioning error using the WLS-NE is represented in black dots (ground truth for covariance).

The conventional solution obtains a mean positioning error of 25.68 meters with a standard deviation of 28.09 meters. With the assistant of the proposed covariance estimation, the mean positioning error drastically decreased to 8.14 meters. The mean positioning error is reduced to 7.49 meters with the covariance magnitude constraint being applied. Moreover, the standard deviation is also decreased to 5.43 meters.

The final optimized nodes and organized point clouds are shown in Fig. 16. The positioning error during the test is shown in Fig. 17. We can see from Fig. 16, the edges of GNSS are dramatically decreased with the constraint of covariance.

Interestingly, the positioning error of all methods decreased after epochs 120. The reason is the detection of the loop closure, which is a strong constraint for further graph-based optimization. Regarding the performance of conventional GNSS/LiDAR integration with no loop closure in the first experiment, the positioning error can still reach about 40 meters at the end of the test.

D. *Discussion*

The proposed GNSS/LiDAR integration method obtained improved performance with the aid of the NLOS exclusion (empowered by LiDAR-based object detection) and the proposed covariance estimation. The proposed NLOS exclusion can obtain improvements when more satellites are available. Though the positioning performance of GNSS is very unsatisfactory during both of the experiments. GNSS is still indispensable for providing the globally referenced positioning.

The proposed covariance estimation can capture the majority of GNSS positioning errors. However, the GNSS positioning error caused by the multipath effect cannot be modeled using the proposed covariance model. In the first experiment, the mean GNSS positioning error is less than 30 meters which is better than the second experiment. This is because the buildings in the second experiment are even taller which introduces more NLOS receptions consequently. As presented in Algorithm 2, only the NLOS is modeled in the covariance. Thus, the second experiment obtains better performance regarding the GNSS covariance estimation which can be seen by comparing the Figs.

TABLE III
EXPERIMENT 2: PERFORMANCE OF THE THREE GNSS/LIDAR INTEGRATION METHODS

All data	Method (a) Conventional GNSS/LiDAR Integration	Method (b) Proposed GNSS/LiDAR Integration	Method (c) Proposed GNSS/LiDAR Integration
Mean Error	25.68 m	8.14 m	7.49 m
STD	28.09 m	6.73 m	5.43 m
Availability	100%	100%	100%

9 and 15. As the multipath effects are random and difficult to model. Thus, effectively modeling of multipath is a promising work to yield.

The proposed constraint of covariance applied to the GNSS/LiDAR integration can improve performance. This novel constraint guarantees that only the accurate GNSS positioning will be applied to the integration. In other words, the effectively estimated covariance can identify the erroneous GNSS results.

In overall, the proposed GNSS covariance estimation can improve the GNSS/LiDAR integration performance. The globally referenced positioning is obtained. This result proves that the covariance estimation is significant for the GNSS/LiDAR integration. However, the integrated positioning result is still large with the best performance of even 7.49 meters of mean error in the second experiment.

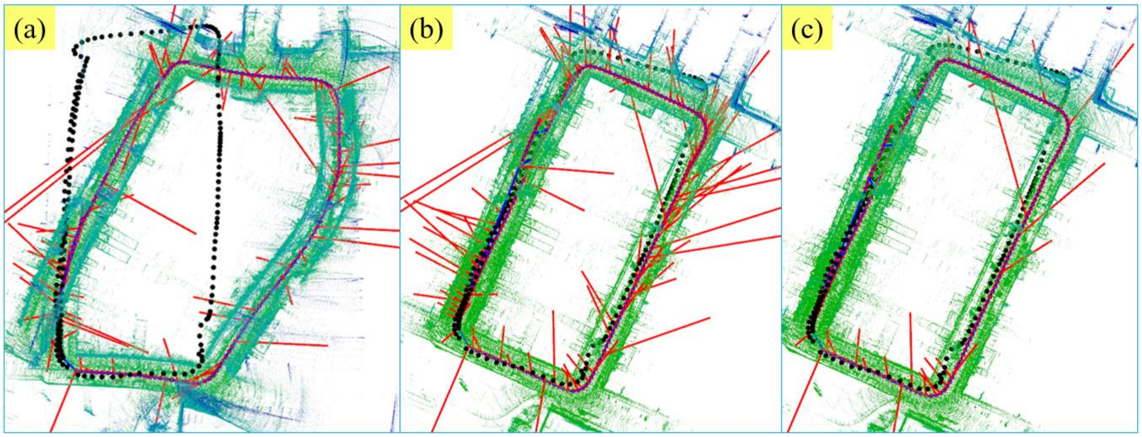

Fig. 16. Experiment 2: Results of the GNSS/LiDAR integration based on three integration methods. The blue curve is constituted by the optimized nodes (refer to the red node in Fig. 6. The black curve indicates the ground truth of the trajectory that provided by NovAtel SPAN-CPT. The red line represents the edge from GNSS positioning: refer to the red line in Fig. 6). The green points represent the organized point clouds.

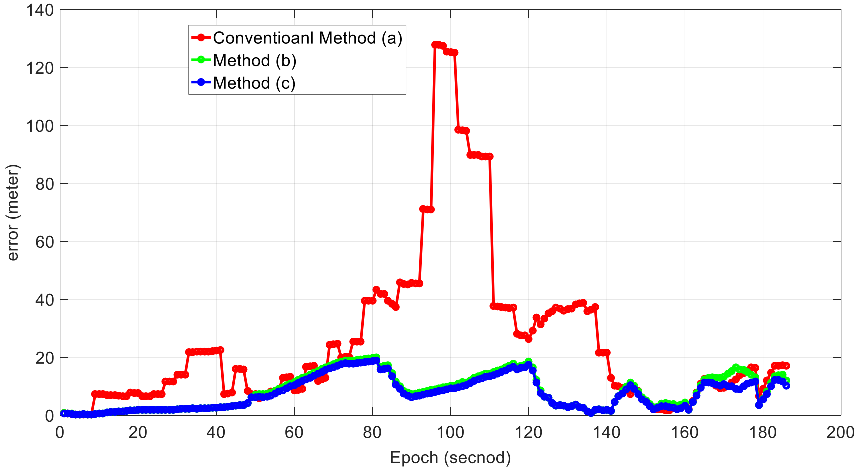

Fig. 17. Experiment 2: Positioning error of the GNSS/LiDAR integration results based on the three methods. Red, green and blue curves indicate the GNSS/LiDAR integration methods (a), (b) and (c), respectively.

To realize autonomous vehicles, this kind of scenario is still a challenge for GNSS positioning. Even the real-time kinematic (RTK) GNSS can suffer from severe NLOS and multipath effects. Direct NLOS exclusion will result in the big distortion of the satellites distribution, namely the HDOP. Thus, effectively modeling the covariance of GNSS positioning is a potential solution to improve the robustness of the GNSS/LiDAR integration in super-urbanized areas.

VI. Conclusions and Future Work

With the fast development of the autonomous vehicles, GNSS and LiDAR became the indispensable sensors to provide sensing and localization functions. The environment feature can be used to improve GNSS positioning performance in urbanized areas with excessive tall buildings. To the best of the author’s knowledge, this paper is the first attempt to employ the LiDAR-based object detection to improve the GNSS.

This paper innovatively employs the LiDAR perception to detect building surface to facilitate the covariance modeling of GNSS positioning for the GNSS/LiDAR integration. This study firstly employs the LiDAR to provide the LiDAR odometry based on the state-of-art NDT and the corresponding covariance is estimated. Then, the building surfaced is detected and identified using the object detection followed by the NLOS detection and novel NLOS exclusion. Thirdly, the GNSS positioning is implemented using the surviving range measurements. The GNSS positioning covariance is proposed based on an NLOS model. Fourthly, the LiDAR odometry and the GNSS positioning is integrated by a graph-based SLAM framework. Finally, the experiment is conducted to validate the propose GNSS/LiDAR integration framework. The results show that the proposed method of GNSS positioning covariance estimation can model the majority of the positioning error caused by NLOS reception. The performance of the proposed GNSS/LiDAR integration with adaptive covariance outperforms the conventional GNSS/LiDAR integration with the constant covariance.

Furthermore, the remaining GNSS positioning error caused by the multipath effects will be studied and modeled to improve the performance of GNSS positioning covariance estimation. Moreover, the real-time kinematic (RTK) GNSS will be applied to integrate with LiDAR to verify how much the proposed method can help the RTK GNSS/LiDAR integration.

ACKNOWLEDGMENT

The authors acknowledge the support of Hong Kong PolyU internal grant on the project G-YBWB, “Research on GPS Error Modelling Using 3D Point Cloud-Based Map for Autonomous Driving Vehicle”. The authors acknowledge and Mr. Sai Hu for his great help in collecting data.

REFERENCES

[1] C. Urmson *et al.*, "Autonomous driving in urban environments: Boss and the urban challenge," *Journal of Field Robotics,* vol. 25, no. 8, pp. 425-466, 2008.

[2] J. Wei, J. M. Snider, J. Kim, J. M. Dolan, R. Rajkumar, and B. Litkouhi, "Towards a viable autonomous driving research platform," in *Intelligent Vehicles Symposium (IV), 2013 IEEE*, 2013, pp. 763-770: IEEE.

[3] B. Douillard *et al.*, "On the segmentation of 3D LIDAR point clouds," in *Robotics and Automation (ICRA), 2011 IEEE International Conference on*, 2011, pp. 2798-2805: IEEE.

[4] W. Li, Q. Guo, M. K. Jakubowski, and M. Kelly, "A new method for segmenting individual trees from the lidar point cloud," *Photogrammetric Engineering & Remote Sensing,* vol. 78, no. 1, pp. 75-84, 2012.

[5] G. Wan, X. Yang, R. Cai, H. Li, H. Wang, and S. Song, "Robust and Precise Vehicle Localization based on Multi-sensor Fusion in Diverse City Scenes," 2017.

[6] S. Thrun, "Probabilistic robotics," *Communications of the ACM,* vol. 45, no. 3, pp. 52-57, 2002.

[7] R. W. Wolcott and R. M. Eustice, "Fast LIDAR localization using multiresolution Gaussian mixture maps," in *Robotics and Automation (ICRA), 2015 IEEE International Conference on*, 2015, pp. 2814-2821: IEEE.

[8] A. Fernández *et al.*, "ATENEA: Advanced techniques for deeply integrated GNSS/INS/LiDAR navigation," in *Satellite Navigation Technologies and European Workshop on GNSS Signals and Signal Processing (NAVITEC), 2010 5th ESA Workshop on*, 2010, pp. 1-8: IEEE.

[9] A. Fernández, P. Silva, and I. Colomina, "Real-time navigation and mapping with mobile mapping systems using LiDAR/Camera/INS/GNSS advanced hybridization algorithms: description and test results," in *Proceedings of the 27th International Technical Meeting of the Satellite Division of the Institute of Navigation, ION GNSS 2014*, 2014, pp. 896-903.

[10] Y. Gao, S. Liu, M. M. Atia, and A. Noureldin, "INS/GPS/LiDAR integrated navigation system for urban and indoor environments using hybrid scan matching algorithm," *Sensors,* vol. 15, no. 9, pp. 23286-23302, 2015.

[11] Y. Gu, L.-T. Hsu, and S. Kamijo, "GNSS/Onboard inertial sensor integration with the aid of 3-d building map for lane-level vehicle self-localization in urban canyon," *IEEE Transactions on Vehicular Technology,* vol. 65, no. 6, pp. 4274-4287, 2016.

[12] X. Zhang, L. Miao, and H. Shao, "Tracking Architecture Based on Dual-Filter with State Feedback and Its Application in Ultra-Tight GPS/INS Integration," *Sensors,* vol. 16, no. 5, p. 627, 2016.

[13] G. P. Huang, A. I. Mourikis, and S. I. Roumeliotis, "Analysis and improvement of the consistency of extended Kalman filter based SLAM," in *Robotics and Automation, 2008. ICRA 2008. IEEE International Conference on*, 2008, pp. 473-479: IEEE.

[14] J. Zhu, N. Zheng, Z. Yuan, Q. Zhang, X. Zhang, and Y. He, "A SLAM algorithm based on the central difference Kalman filter," in *Intelligent Vehicles Symposium, 2009 IEEE*, 2009, pp. 123-128: IEEE.

[15] C. Cadena and J. Neira, "SLAM in O (logn) with the Combined Kalman-Information Filter," *Robotics and Autonomous Systems,* vol. 58, no. 11, pp. 1207-1219, 2010.

[16] S. Thrun and Y. Liu, "Multi-robot SLAM with sparse extended information filers," in *Robotics Research. The Eleventh International Symposium*, 2005, pp. 254-266: Springer.

[17] J.-S. Gutmann, E. Eade, P. Fong, and M. Munich, "A constant-time algorithm for vector field slam using an exactly sparse extended information filter," *Robotics: Science and Systems VI,* p. 193, 2011.

[18] D. Törnqvist, T. B. Schön, R. Karlsson, and F. Gustafsson, "Particle filter SLAM with high dimensional vehicle model," *Journal of Intelligent and Robotic Systems,* vol. 55, no. 4-5, pp. 249-266, 2009.

[19] N. Fairfield, G. Kantor, and D. Wettergreen, "Towards particle filter SLAM with three dimensional evidence grids in a flooded subterranean environment," in *Robotics and Automation, 2006. ICRA 2006. Proceedings 2006 IEEE International Conference on*, 2006, pp. 3575-3580: IEEE.

[20] R. Sim, P. Elinas, and J. J. Little, "A study of the Rao-Blackwellised particle filter for efficient and accurate vision-based SLAM," *International Journal of Computer Vision,* vol. 74, no. 3, pp. 303-318, 2007.

[21] S. Thrun, W. Burgard, and D. Fox, *Probabilistic robotics*. MIT press, 2005.

[22] F. Dellaert and M. Kaess, "Square Root SAM: Simultaneous localization and mapping via square root information smoothing," *The International Journal of Robotics Research,* vol. 25, no. 12, pp. 1181-1203, 2006.

[23] F. Lu and E. Milios, "Globally consistent range scan alignment for environment mapping," *Autonomous robots,* vol. 4, no. 4, pp. 333-349, 1997.

[24] E. Olson, J. Leonard, and S. Teller, "Fast iterative alignment of pose graphs with poor initial estimates," in *Robotics and Automation, 2006. ICRA 2006. Proceedings 2006 IEEE International Conference on*, 2006, pp. 2262-2269: IEEE.

[25] T. Sakai, K. Koide, J. Miura, and S. Oishi, "Large-scale 3D outdoor mapping and on-line localization using 3D-2D matching," in *System Integration (SII), 2017 IEEE/SICE International Symposium on*, 2017, pp. 829-834: IEEE.

[26] G. Grisetti, R. Kummerle, C. Stachniss, and W. Burgard, "A tutorial on graph-based SLAM," *IEEE Intelligent Transportation Systems Magazine,* vol. 2, no. 4, pp. 31-43, 2010.

[27] L.-T. Hsu, "Analysis and modeling GPS NLOS effect in highly urbanized area," *GPS solutions,* vol. 22, no. 1, p. 7, 2018.

[28] J. Breßler, P. Reisdorf, M. Obst, and G. Wanielik, "GNSS positioning in non-line-of-sight context—A survey," in *Intelligent Transportation Systems (ITSC), 2016 IEEE 19th International Conference on*, 2016, pp. 1147-1154: IEEE.

[29] M. Adjrad and P. D. Groves, "Intelligent Urban Positioning: Integration of Shadow Matching with 3D-Mapping-Aided GNSS Ranging," *The Journal of Navigation,* vol. 71, no. 1, pp. 1-20, 2018.

[30] P. D. Groves, "Shadow matching: A new GNSS positioning technique for urban canyons," *The journal of Navigation,* vol. 64, no. 3, pp. 417-430, 2011.

[31] L.-T. Hsu, Y. Gu, Y. Huang, and S. Kamijo, "Urban pedestrian navigation using smartphone-based dead reckoning and 3-D map-aided GNSS," *IEEE Sensors Journal,* vol. 16, no. 5, pp. 1281-1293, 2016.

[32] L.-T. Hsu, Y. Gu, and S. Kamijo, "3D building model-based pedestrian positioning method using GPS/GLONASS/QZSS and its reliability calculation," *GPS solutions,* vol. 20, no. 3, pp. 413-428, 2016.

[33] S. Miura, L.-T. Hsu, F. Chen, and S. Kamijo, "GPS error correction with pseudorange evaluation using three-dimensional maps," *IEEE Transactions on Intelligent Transportation Systems,* vol. 16, no. 6, pp. 3104-3115, 2015.

[34] P. François, B. David, and M. Florian, "Non-Line-Of-Sight GNSS signal detection using an on-board 3D model of buildings," in *ITS Telecommunications (ITST), 2011 11th International Conference on*, 2011, pp. 280-286: IEEE.

[35] P. D. Groves, Z. Jiang, L. Wang, and M. K. Ziebart, "Intelligent urban positioning using multi-constellation GNSS with 3D mapping and NLOS signal detection," 2012.

[36] S. Peyraud *et al.*, "About non-line-of-sight satellite detection and exclusion in a 3D map-aided localization algorithm," *Sensors,* vol. 13, no. 1, pp. 829-847, 2013.

[37] F. Peyret, D. Bétaille, P. Carolina, R. Toledo-Moreo, A. F. Gómez-Skarmeta, and M. Ortiz, "Gnss autonomous localization: Nlos satellite detection based on 3-d maps," *IEEE Robotics & Automation Magazine,* vol. 21, no. 1, pp. 57-63, 2014.

[38] D. Bétaille, F. Peyret, and M. Voyer, "Applying standard digital map data in map-aided, lane-level GNSS location," *The Journal of navigation,* vol. 68, no. 5, pp. 827-847, 2015.

[39] M. Obst, S. Bauer, P. Reisdorf, and G. Wanielik, "Multipath detection with 3D digital maps for robust multi-constellation GNSS/INS vehicle localization in urban areas," in *Intelligent Vehicles Symposium (IV), 2012 IEEE*, 2012, pp. 184-190: IEEE.

[40] M. Hentschel, O. Wulf, and B. Wagner, "A GPS and laser-based localization for urban and non-urban outdoor environments," in *Intelligent Robots and Systems, 2008. IROS 2008. IEEE/RSJ International Conference on*, 2008, pp. 149-154: IEEE.

[41] D. Maier and A. Kleiner, "Improved GPS sensor model for mobile robots in urban terrain," in *Robotics and Automation (ICRA), 2010 IEEE International Conference on*, 2010, pp. 4385-4390: IEEE.

[42] A. P. Shetty, "GPS-LiDAR sensor fusion aided by 3D city models for UAVs," 2017.

[43] W. Wen, G. Zhang, and L.-T. Hsu, "Exclusion of GNSS NLOS Receptions Caused by Dynamic Objects in Heavy Traffic Urban Scenarios Using Real-Time 3D Point Cloud: An Approach without 3D Maps," *arXiv preprint arXiv:1804.10917,* 2018.

[44] J. Marshall, "Creating and viewing skyplots," *GPS solutions,* vol. 6, no. 1-2, pp. 118-120, 2002.

[45] J. Zhang and S. Singh, "LOAM: Lidar Odometry and Mapping in Real-time," in *Robotics: Science and Systems*, 2014, vol. 2.

[46] D. Chetverikov, D. Stepanov, and P. Krsek, "Robust Euclidean alignment of 3D point sets: the trimmed iterative closest point algorithm," *Image and Vision Computing,* vol. 23, no. 3, pp. 299-309, 2005.

[47] M. Magnusson, A. Lilienthal, and T. Duckett, "Scan registration for autonomous mining vehicles using 3D‐NDT," *Journal of Field Robotics,* vol. 24, no. 10, pp. 803-827, 2007.

[48] M. Magnusson, "The three-dimensional normal-distributions transform: an efficient representation for registration, surface analysis, and loop detection," Örebro universitet, 2009.

[49] M. Magnusson, H. Andreasson, A. Nuchter, and A. J. Lilienthal, "Appearance-based loop detection from 3D laser data using the normal distributions transform," in *Robotics and Automation, 2009. ICRA'09. IEEE International Conference on*, 2009, pp. 23-28: IEEE.

[50] W. Wen, G. Zhang, and L.-T. Hsu, "Exclusion of GNSS NLOS receptions caused by dynamic objects in heavy traffic urban scenarios using real-time 3D point cloud: An approach without 3D maps," in *Position, Location and Navigation Symposium (PLANS), 2018 IEEE/ION*, 2018, pp. 158-165: IEEE.

[51] *GNSS Satellites system*. Available: https://www.gislounge.com/global-navigation-satellite-systems/

[52] E. Realini and M. Reguzzoni, "goGPS: open source software for enhancing the accuracy of low-cost receivers by single-frequency relative kinematic positioning," *Measurement Science and technology,* vol. 24, no. 11, p. 115010, 2013.

[53] E. Kaplan and C. Hegarty, *Understanding GPS: principles and applications*. Artech house, 2005.

[54] R. Kümmerle, G. Grisetti, H. Strasdat, K. Konolige, and W. Burgard, "g 2 o: A general framework for graph optimization," in *Robotics and Automation (ICRA), 2011 IEEE International Conference on*, 2011, pp. 3607-3613: IEEE.

[55] W. Wen, L.-T. Hsu, and G. Zhang, "Performance analysis of NDT-based graph SLAM for autonomous vehicle in diverse typical driving scenarios of Hong Kong," *Sensors,* vol. 18, no. 11, p. 3928, 2018.

[56] M. Quigley *et al.*, "ROS: an open-source Robot Operating System," in *ICRA workshop on open source software*, 2009, vol. 3, no. 3.2, p. 5: Kobe, Japan.

[57] P. D. Groves, *Principles of GNSS, inertial, and multisensor integrated navigation systems*. Artech house, 2013.

Weisong WEN was born in Ganzhou, Jiangxi, China. He is a Ph.D. candidate in mechanical engineering, the Hong Kong Polytechnic University. His research interests include the GNSS/INS/LiDAR/HD Map-based localization for autonomous vehicles. He is currently a visiting student researcher in University of California, Berkeley (UCB).

Guohao Zhang received the bachelor’s degree in mechanical engineering and Automation from University of Science and Technology Beijing, China, in 2015. He received the master’s degree in mechanical engineering and currently is a research assistant in the Hong Kong Polytechnic University. His research interests including GNSS urban localization, vehicle-to-vehicle cooperative localization and multi-sensor integrated navigation.

Li-Ta Hsu received the B.S. and Ph.D. degrees in aeronautics and astronautics from National Cheng Kung University, Taiwan, in 2007 and 2013, respectively. He is currently an assistant professor with Interdisciplinary Division of Aeronautical and Aviation Engineering, The Hong Kong Polytechnic University, before he served as post-doctoral researcher in Institute of Industrial Science at University of Tokyo, Japan. In 2012, he was a visiting scholar in University College London, U.K. His research interests include GNSS positioning in challenging environments and localization for pedestrian, autonomous driving vehicle and unmanned aerial vehicle.